Filtered backprojection for thermoacoustic computed tomography in spherical geometry

(Published in: M3AS 28(16): 1919-1937, 2005)

M. Haltmeier[1] and T. Schuster[2] and O. Scherzer[1]

[1] Department of Computer Science, Universität Innsbruck, Technikerstraße 21a, A-6020 Innsbruck, Austria.
Markus.Haltmeier@uibk.ac.at, Otmar.Scherzer@uibk.ac.at.
[2] Fachrichtung Mathematik, Geb. 36, Universität des Saarlandes, 66041 Saarbrücken, Germany.
Thomas.Schuster@num.uni-sb.de.

November 3, 2012

Abstract

Thermoacoustic computed tomography (TCT) is a novel imaging technique for nondestructive evaluation and medical imaging. It uses electromagnetic energy as input and the induced thermoacoustic pressure field as measurement output. The determination of the unknown energy deposition function is based on the integral geometric problem of reconstructing a function from its integrals over certain spheres. We apply the method of approximate inverse to derive filtered backprojection type reconstruction algorithms in spherical scanning geometry. Numerical results are presented and show the validity of the resulting algorithms.

1 Introduction

Current research demonstrates that thermoacoustic computed tomography (TCT) is a promising hybrid imaging technique for nondestructive evaluation and medical imaging. It combines the advantages of purely optical imaging (high contrast) and ultrasound imaging (high resolution). It uses either pulsed radio frequency or pulsed laser as energy input and measures the induced thermoacoustic pressure field [11, 12, 28, 7].

Assume a semitransparent sample is illuminated by a pulsed electromagnetic energy. The specific properties of the absorbing medium result in a nonuniform energy deposition within the sample, followed by a nonuniform thermoelastic expansion. This produces an acoustic pressure wave [6, 14]. At some specified frequencies of the electromagnetic radiation different tissues offer a highly varying absorptivity, which establishes the potentiality of high contrast imaging [9]. The goal of TCT is to recover the significant energy deposition by measuring the induced thermoacoustic pressure wave using acoustic detectors located outside the illuminated sample.

If the duration of the electromagnetic pulse is short and the acoustic properties of the illuminated sample are relatively homogeneous, the generated thermoacoustic time-dependent pressure at a point $x \in \mathbb{R}^3$ is essentially given by the integral of the energy deposition function over spheres centered at x.

In mathematical terms TCT consists in the problem of recovering the energy deposition function from its mean values over spheres with centers lying on a hypersurface S (location of the detectors). Typically the center set S is either a plane, a sphere or a cylinder [27, 28, 29, 10, 11]. In this paper we consider the case where the center set is a sphere and apply the method of approximate inverse to derive filtered backprojection type reconstruction algorithms.

The outline of this work is as follows: in section 2 we recall the physical principles of linear thermoacoustics. Thermoacoustic tomography in spherical scanning geometry is addressed in section 3. The method of approximate inverse is outlined in section 4 and applied to TCT in section 5. We derive novel reconstruction algorithms similar to those used in ordinary x-ray computed tomography. Finally, results of our numerical studies are presented in section 6.

2 Linear Thermoacoustics

In this section we illustrate the basic physical principles of linear thermoacoustics. The governing equations of linear thermoacoustics are the linearized balance equations of fluid dynamics [13, 4] for a *homogeneous*, *isotropic*, *inviscid* fluid and an additional equation relating the change of thermal energy to the change of electromagnetic radiation.

The *linearized continuity equation*

$$\frac{\partial \varrho}{\partial \hat{t}} = -\varrho_0 \nabla \cdot \mathbf{v}\,, \tag{1}$$

is derived from the principle of *conservation of mass* if the *particle velocity* $\mathbf{v}(x,\hat{t})$ is small and the *mass density* $\varrho_{\text{tot}}(x,\hat{t}) = \varrho_0 + \varrho(x,\hat{t})$ is weakly varying, i.e., $|\varrho(x,\hat{t})| \ll \varrho_0$.

The *linearized Euler equation*

$$\varrho_0 \frac{\partial \mathbf{v}}{\partial \hat{t}} = -\nabla p\,, \tag{2}$$

is derived from the principle of *conservation of momentum* for a *non-viscous*, *non-turbulent* flow in the absence of external forces with slowly varying *pressure* $p_{\text{tot}}(x,\hat{t}) = p_0 + p(x,\hat{t})$, i.e., $|p(x,\hat{t})| \ll p_0$, within the fluid [2]. By combining equations (1) and (2) we can eliminate the particle velocity and find

$$\frac{\partial^2 \varrho}{\partial \hat{t}} - \triangle p = 0\,. \tag{3}$$

To relate the mass density and the pressure to the absorbed electromagnetic energy we assume the existence of the so called *entropy density function* $s_{\text{tot}}(x,\hat{t}) = s_0 + s(x,\hat{t})$ with $|s(x,\hat{t})| \ll s_0$ such that the following two properties hold:

1. The *internal energy* can be written as a function $e_{\text{tot}} = \hat{e}(s_{\text{tot}}, \varrho_{\text{tot}})$ of mass density and entropy.

2. The pressure is given by the change of internal energy with respect to the volume

$$p_{\text{tot}} = \hat{p}(s_{\text{tot}}, \varrho_{\text{tot}}) := \frac{1}{\varrho_{\text{tot}}^2} \frac{\partial \hat{e}}{\partial \varrho}(s_{\text{tot}}, \varrho_{\text{tot}})\,. \tag{4}$$

Usually the *temperature* is defined as the rate of change of internal energy with respect to entropy

$$T_{\text{tot}} := \hat{T}(s_{\text{tot}}, \varrho_{\text{tot}}) := \frac{\partial \hat{e}}{\partial s}(s_{\text{tot}}, \varrho_{\text{tot}})\,,$$

and we assume that $|T_{\text{tot}} - T_0| \ll T_0$ whereby $T_0 := \hat{T}(s_0, \varrho_0)$.

The *linearized entropy equation*

$$\varrho_0 T_0 \frac{\partial s}{\partial \hat{t}} = r\,,$$

is derived from the principle of *conservation of energy* under the assumption that the *heat flux* is negligible. Here $r(x,\hat{t})$ denotes the absorbed energy per unit volume and unit time. The absorbed energy

$$r(x,\hat{t}) = \hat{I}_{\text{em}}(x) j(\hat{t}) \psi(x)\,,$$

is proportional to the electromagnetic *radiation intensity* $\hat{I}_{\text{em}}(x)j(t)$ and the absorbtion density $\psi(x)$ inside the fluid. The temporal shape of the electromagnetic pulse $j(t) \in C^1(\mathbb{R})$ is assumed to have small support $[0,\tau]$ ($\tau \ll 1$), to be non-negative, and to satisfy

$$\int_{\mathbb{R}} j(\hat{t}) d\hat{t} = 1\,.$$

Such a function approximates the δ-distribution.

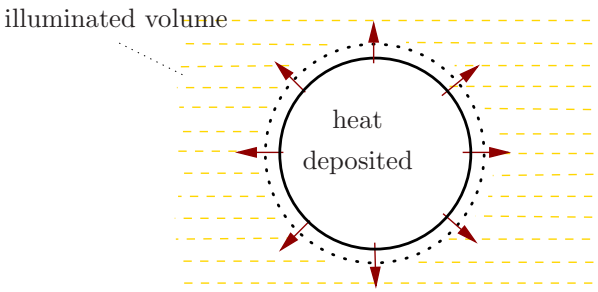

Figure 1: Thermoelastic effect. The absorbed electromagnetic energy within the illuminated part of the fluid causes thermal expansion and a subsequent pressure field. The dependance between the thermoelastic expansion and the pressure on the received electromagnetic energy is given by the expansion equation (6).

From equation (4) it follows that

$$\frac{\partial s}{\partial \hat{t}} = \frac{\partial p/\partial \hat{t}}{\partial \hat{p}/\partial s} - \frac{(\partial \hat{p}/\partial \varrho)(\partial \varrho/\partial \hat{t})}{\partial \hat{p}/\partial s}\,. \tag{5}$$

Here $\partial \hat{p}/\partial s$ and $\partial \hat{p}/\partial \varrho$ denote the first partial derivatives of $\hat{p}$. The *specific heat capacity* c_p, the *thermal expansion coefficient* at constant pressure β, and the adiabatic *speed of sound* v_s are given by the following relations (see e.g.[6])

$$\frac{\partial \hat{p}}{\partial \varrho} = v_s^2 \qquad \text{and} \qquad \frac{\partial \hat{p}}{\partial s} = \frac{T_0 v_s^2 \varrho_0 \beta}{c_p}\,.$$

Inserting these identities into equation (5) and expressing $\partial s/\partial \hat{t}$ in accordance with the linearized entropy equation it follows that

$$\frac{\partial \varrho}{\partial \hat{t}} = \frac{1}{v_s^2}\frac{\partial p}{\partial \hat{t}} - \frac{\beta}{c_p} r\,. \tag{6}$$

Equation (6) is called *expansion equation* since it describes the relation between the rate of change of volume to the change of pressure and the deposited energy per unit time. Together with (6) and a scaling of time $t = \hat{t} v_s$ equation (3) implies

$$\left(\frac{\partial^2}{\partial t^2} - \triangle\right) p = f(x)\frac{dj}{dt}\,, \tag{7}$$

where

$$f(x) := \frac{\beta v_s}{c_p}\hat{I}_{\mathrm{em}}(x)\psi(x)$$

is the normalized *energy deposition* function.

The solution of (7) is unique if appropriate initial conditions are specified. We use

$$p(x,0) = 0\,, \quad \text{together with} \quad \frac{\partial p}{\partial t}(x,0) = 0\,, \tag{8}$$

to represent the fact that there is no acoustic pressure before the beginning of the experiment (at time $\hat{t} = 0$). The unique solution of (7) and (8) is given by

$$p := \frac{dj}{dt} *_t (t\,\mathbf{M}f)\,, \tag{9}$$

where $*_t$ is the (Laplace-) convolution

$$(g_1 *_t g_2)(x,t) := \int_0^t g_1(x, t-s) g_2(x,s)\, ds$$

with respect to t and $\mathbf{M}f$ is the spherical mean operator

$$(\mathbf{M}f)(x,t) := \frac{1}{4\pi}\int_{S^2} f(x+t\omega)d\Omega(\omega) \tag{10}$$

for $t \geq 0$ and $x \in \mathbb{R}^3$ (see e.g. [8, p. 136]). Here S^2 denotes the two-dimensional unit sphere in $\mathbb{R}^3$ with surface measure $d\Omega$.

In mathematical terms thermoacoustic tomography is concerned with the inverse problem of recovering an unknown energy deposition function f from temporal measurement data of the thermoacoustic pressure field p taken on a surface S outside the illuminated fluid.

3 Thermoacoustic tomography in spherical scanning geometry

In this section we explicitly deal with the case where the energy deposition function f is supported in a closed ball $B_\rho := \overline{B_\rho(0)}$ with center 0 and radius ρ and in which the thermoacoustic pressure field is measured on $S_\rho := \partial B_\rho$.

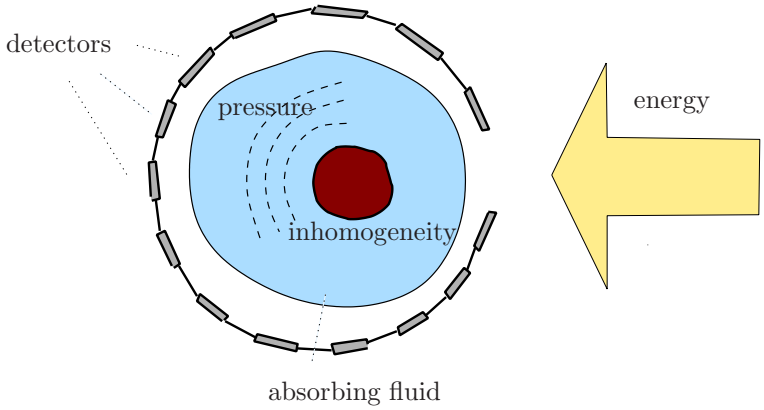

Figure 2: Thermoacoustic scanning system. The examined object is illuminated by a short electromagnetic pulse. The *thermoelastic effect* (c.f. figure 1) causes an evolving pressure wave that is measured with several acoustic detectors enclosing the imaged object.

The following notations will hold throughout the paper:

$$X := L^2(B_\rho) = \{f \in L^2(\mathbb{R}^3) : f(x) = 0 \text{ for a.e. } x \in \mathbb{R}^3 \setminus B_\rho\}$$

denotes the Hilbert space of all square integrable functions supported in B_ρ with associated inner product $\langle\cdot,\cdot\rangle$ and norm $\|\cdot\|$. For all $T \geq 0$ let

$$Y_T := L^2(S_\rho \times [0,T])\,,$$

denote the Hilbert space of all square integrable functions $f : S_\rho \times [0,\infty) \to \mathbb{R}$ supported in $S_\rho \times [0,T]$. We denote by

$$\langle g_1, g_2\rangle_T = \int_{S_\rho}\int_0^T g_1(\sigma,t)g_2(\sigma,t)\,dt\,d\Omega_\rho(\sigma)$$

its inner product and by $\|\cdot\|_T$ the associated norm. Here $d\Omega_\rho$ denotes the surface measure on S_ρ. Let D_t be the operator that maps $\varphi \in C^1(S_\rho \times [0,\infty))$ onto its derivative with respect to the second variable:

$$D_t\varphi(y,t) = \varphi_t(y,t)\,, \qquad y \in S_\rho\,, \quad t \in [0,\infty)\,.$$

Finally we introduce the operators

$$\begin{aligned} \mathbf{N} : C_c^0(B_\rho) \subseteq X &\to Y_{2\rho}\,, \qquad (\mathbf{N}f)(\sigma,t) := t\mathbf{M}f(\sigma,t)\,, \\ \mathbf{P} : C_c^0(B_\rho) \subseteq X &\to Y_{2\rho+\tau}\,, \quad \mathbf{P}f = D_t j *_t \mathbf{N}f\,. \end{aligned}$$

From (9) we see that the operator $\mathbf{P}$ maps an unknown energy deposition function f onto the thermoacoustic pressure field restricted to the recording surface S_ρ. Particularily, if f is a C^1 function and the pulse duration τ tends to 0 then $\mathbf{P}f$ tends to $D_t\mathbf{N}f$.

Lemma 3.1. *Let $f \in C_c^0(B_\rho)$. Then $\|\mathbf{N}f\|_{2\rho}^2 \le \rho^2\|f\|^2$ and*

$$\|\mathbf{P}f\|_{2\rho+\tau}^2 \le (2\rho+\tau)\tau\rho^2\|D_t j\|_\infty^2\|f\|^2\,. \tag{11}$$

Here $\|D_t j\|_\infty := \sup\{|D_t j(t)| : 0 \le t \le \tau\}$ denotes the supremum norm of $D_t j$.

Proof. Let $\sigma \in S_\rho$. Since $\mathrm{supp}(f) \subseteq B_\rho$ it follows from the Cauchy inequality that

$$\begin{aligned} \|\mathbf{N}f(\sigma,\cdot)\|_{L^2[0,2\rho]}^2 &= \int_0^{2\rho}\left(\frac{t}{4\pi}\int_{S^2} f(\sigma+t\omega)d\Omega(\omega)\right)^2 dt \\ &\le \frac{1}{4\pi}\int_0^{2\rho}\int_{S^2} f(\sigma+t\omega)^2 d\Omega(\omega)\, t^2\, dt \;=\; \frac{1}{4\pi}\|f\|^2\,. \end{aligned}$$

This shows that

$$\|\mathbf{N}f\|_{2\rho}^2 = \int_{S_\rho}\|\mathbf{N}f(\sigma,\cdot)\|_{L^2[0,2\rho]}^2\, d\Omega_\rho(\sigma) \le \rho^2\|f\|^2\,. \tag{12}$$

Next we verify (11). Assume $y \in S_\rho$ and $t \in [0, 2\rho+\tau]$. A further application of the Cauchy inequality yields

$$\begin{aligned} |D_t j *_t \mathbf{N}f(\sigma,t)|^2 &= \left[\int_0^t \mathbf{N}f(\sigma,t-s)(D_t j)(s)\, ds\right]^2 \\ &\le \|\mathbf{N}f(\sigma,\cdot)\|_{L^2[0,2\rho]}^2\int_0^\tau (D_t j)(s)^2\, ds \le \tau\|D_t j\|_\infty^2\|\mathbf{N}f(\sigma,\cdot)\|_{L^2[0,2\rho]}^2\,. \end{aligned}$$

From the last inequality and (12) we conclude that

$$\begin{aligned} \|\mathbf{P}f\|_{2\rho+\tau}^2 &= \int_{S_\rho}\int_0^{2\rho+\tau} |D_t j * \mathbf{N}f(\sigma,t)|^2\, dt\, d\Omega(y) \\ &\le (2\rho+\tau)\tau\|D_t j\|_\infty^2\int_{S_\rho}\|\mathbf{N}f(\sigma,\cdot)\|_{L^2[0,\tau]}^2 \\ &\le (2\rho+\tau)\tau\|D_t j\|_\infty^2\rho^2\|f\|^2\,. \end{aligned}$$

Hence we have shown (11). □

As a consequence of lemma 3.1 the operators $\mathbf{N}$ and $\mathbf{P}$ extend in a unique way to bounded linear operators $\mathbf{N} : X \to Y_{2\rho}$ and $\mathbf{P} : X \to Y_{2\rho+\tau}$, respectively. In particular they have bounded adjoints.

Lemma 3.2. *Let $g \in C_c^0(S_\rho \times [0,2\rho])$ and $p \in C_c^0(S_\rho \times [0, 2\rho+\tau])$. Then,*

$$(\mathbf{N}^* g)(x) = \frac{1}{4\pi}\int_{S_\rho}\frac{g(x,\|x-\sigma\|)}{\|x-\sigma\|}\, d\Omega_\rho(\sigma)\,, \qquad x \in B_\rho\,, \tag{13}$$

$$(\mathbf{P}^* p)(x) = -\frac{1}{4\pi}\int_{S_\rho}\frac{(D_t\bar{j} \star p)(x,\|x-\sigma\|)}{\|x-\sigma\|}\, d\Omega_\rho(\sigma)\,, \qquad x \in B_\rho\,. \tag{14}$$

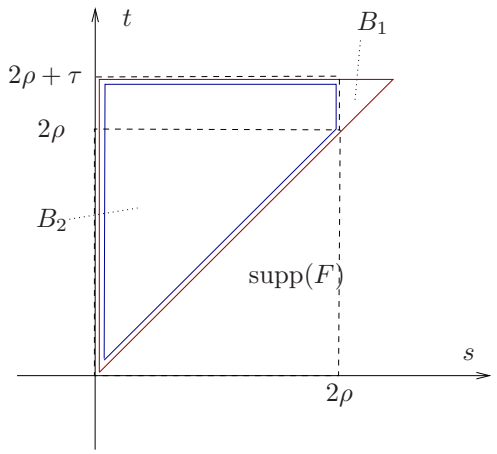

Figure 3: The intersection of the support of the function $D_t j(t-s)$ with $\mathrm{supp}(F)$ is contained in $B_2 \subseteq B_1$.

Here $\bar{j}$ *is defined by* $\bar{j}(s) := j(-s)$ *and*

$$(D_t\bar{j} \star p)(x,s) := \int_s^{s+\tau} D_t\bar{j}(s-t)p(x,t)\,dt\,.$$

Proof. Let $f \in C_c^0(B_\rho)$ and $g \in C_c^0(S_\rho \times [0,2\rho])$. We verify equation (13) by showing that $\langle \mathbf{N}f, g\rangle_{2\rho} = \langle f, \mathbf{N}^* g\rangle$. From Fubini's theorem we obtain

$$\begin{aligned}
\langle \mathbf{N}f, g\rangle_{2\rho} &= \int_{S_\rho}\int_0^{2\rho} t\mathbf{M}f(\sigma,t)g(\sigma,t)\,dt\,d\Omega_\rho(\sigma) \\
&= \frac{1}{4\pi}\int_0^{2\rho}\int_{S^2}\int_{S_\rho} f(\sigma+t\omega)g(\sigma,t)\,d\Omega(\sigma)\,d\Omega_\rho(\omega)\,t\,dt \\
&= \frac{1}{4\pi}\int_{B_\rho} f(x)\int_{S_\rho}\frac{g(\sigma,\|x-\sigma\|)}{\|x-\sigma\|}\,d\Omega_\rho(\sigma)\,dx\,,
\end{aligned}$$

where the last equality follows by the substituting $x = \sigma + t\omega$. Hence we proved (13).

Next we verify equation (14). Let $f \in C_c^0(B_\rho)$ and $p \in C_c^0(S_\rho \times [0,2\rho+\tau])$. Moreover, let $y \in S_\rho$ and define

$$\begin{aligned}
B_1 &:= \bigcup_{0\le t\le 2\rho+\tau} [0,t]\times\{t\}\,, \\
B_2 &:= \bigcup_{0\le s\le 2\rho} \{s\}\times[s,2\rho+\tau]\,.
\end{aligned}$$

Clearly $B_2 \subseteq B_1$. Since $(\mathbf{N}f)(\sigma,\cdot)$ is supported in $[0,2\rho]$ the function $F(s,t) := (\mathbf{N}f)(\sigma,s)p(y,t)$ vanishes on the complement of B_2 (see figure 3). Hence Fubini's theorem gives

$$\begin{aligned}
\int_0^{2\rho+\tau}(D_t j *_t \mathbf{N}f)(\sigma,\cdot)\,p(\sigma,t)\,dt &= \int_0^{2\rho+\tau}\int_0^t D_t j(t-s)\mathbf{N}f(\sigma,s)\,p(\sigma,t)\,ds\,dt \\
&= \int_{B_1}(D_t j)(t-s)\mathbf{N}f(\sigma,s)p(\sigma,t)\,d(s,t) \\
&= \int_{B_2}(D_t j)(t-s)\mathbf{N}f(\sigma,s)p(\sigma,t)\,d(s,t) \\
&= \int_0^{2\rho}\mathbf{N}f(\sigma,s)\int_s^{2\rho+\tau}(D_t j)(t-s)p(\sigma,t)\,dt\,ds\,.
\end{aligned}$$

Since $(D_t\bar{j})(t) = -(D_t j)(-t)$ the last equality together with (13) implies that

$$\begin{aligned}\langle \mathbf{P}f, p\rangle_{2\rho+\tau} &= \int_{S_\rho}\int_0^{2\rho+\tau} (D_t j *_t \mathbf{N}f)(\sigma,t)p(\sigma,t)\,dt\,d\Omega_\rho(\sigma)\\ &= -\int_{S_\rho}\int_0^{2\rho} \mathbf{N}f(\sigma,s)\int_s^{s+\tau}(D_t\bar{j})(s-t)p(\sigma,t)\,dt\,ds\,d\Omega_\rho(\sigma)\\ &= -\int_{S_\rho}\int_0^{2\rho} \mathbf{N}f(\sigma,s)(D_t\bar{j}\star p)(\sigma,s)\,ds\,d\Omega(\sigma) = \langle f, \mathbf{P}^* p\rangle\,,\end{aligned}$$

where $\mathbf{P}^*g$ is defined by (14). □

Remark 3.3. *The duration τ of the electromagnetic pulse is typically in the range of micro seconds. Hence the temporal part of the electromagnetic pulse can be approximated by the delta distribution. Therefore we can regard $D_t\mathbf{N}f$ as measurement data. From lemma 3.2 it follows that we can approximate its adjoint suitable by $-\mathbf{N}^*D_t p$.*

In a recent paper Finch et al [5] proved the injectivity of the operator $\mathbf{N}$ on the space of smooth (i.e. C^∞) functions that are supported in B_ρ. Moreover in [5] several inversion formulas have been stated and proven.

Theorem 3.4. *[5, Theorem 3] Let $f \in C_c^\infty(B_\rho)$. Then*

$$f = -\frac{2}{\rho}\mathbf{N}^* D_t t D_t \mathbf{N} f\,. \tag{15}$$

For our purposes in Sections 5 and 6 have to extend this formula to non-smooth functions.

Corollary 3.5. *Let $f \in C_c^1(B_\rho)$ and assume $D_t\mathbf{N}f \in C_c^1(S_\rho \times [0,2\rho])$. Then (15) holds true.*

Proof. Let $\varphi \in C_c^\infty(B_\rho)$. From theorem 3.4 it follows that (15) holds true for φ and hence $-\rho/2\langle f,\varphi\rangle = \langle f, \mathbf{N}^* D_t t D_t \mathbf{N}\varphi\rangle$. Since f and hence $\mathbf{N}^*f$ is a C^1 function the right hand side of this equation is given by $-\langle tD_t\mathbf{N}f, D_t\mathbf{N}\varphi)\rangle_{2\rho}$. Together with the assumption $D_t\,\mathbf{N}f \in C_c^1(S_\rho\times[0,2\rho])$ this implies that

$$-\frac{\rho}{2}\langle f,\varphi\rangle = \langle \mathbf{N}^* D_t t D_t \mathbf{N} f, \varphi\rangle\ .$$

Since the last equality is valid for all $\varphi \in C_c^\infty(B_\rho)$ we can conclude that $-\rho/2 f = \mathbf{N}^* D_t t D_t \mathbf{N} f$. □

4 Approximate Inverse for linear operator equations

The method of approximate inverse is a regularization scheme which has been developed for a stable solution of operation equations of the first kind

$$\mathbf{A}f = g \tag{16}$$

in Hilbert spaces. Since its establishment by Louis, Maaß [18], Louis [15, 16] the method has led to novel and efficient solvers in such different applications as 2D- and 3D- computerized tomography [19, 17], vector field tomography [23, 24, 22], inverse scattering [1], sonar [26] and x-ray diffractometry [25].

Let $\mathbf{A}$ in (16) be a linear, bounded operator between function spaces $X := L^2(\Omega_1,\mu_1)$ and $Y := L^2(\Omega_2,\mu_2)$ where $\Omega_i \subset \mathbb{R}^{n_i}$, $i = 1,2$, are bounded domains. Further assume $e \in X$ to be a continuous function satisfying

$$\int_{\mathbb{R}^{n_1}} e(x)\,dx = 1\,, \tag{17}$$

and define for $\gamma > 0$

$$e_\gamma(x,y) = \gamma^{-n_1}\, e\Big((x-y)/\gamma\Big)\,. \tag{18}$$

If e_γ satisfies

$$\int_{\Omega_1} f(x)\, e_\gamma(x,y)\, dx \to f(y)\,, \quad a.e.\,, \tag{19}$$

in X when $\gamma \to 0$, we call e a *mollifier*. The idea of approximate inverse consists of computing the smoothed version

$$f_\gamma(y) := \langle f, e_\gamma(\cdot,y)\rangle_X \tag{20}$$

rather than f itself. To get a representation of f_γ which does not depend on the exact solution f we consider the dual equation

$$\mathbf{A}^* v_\gamma(y) = e_\gamma(\cdot,y) \tag{21}$$

and assume for the moment that $e_\gamma(\cdot,y)$ is in the range of $\mathbf{A}^*$, the L^2-adjoint of $\mathbf{A}$, for $y \in \Omega_1$. Having the solution $v_\gamma(y)$ of (21) at hand we obtain with (20)

$$f_\gamma(y) = \langle f, \mathbf{A}^* v_\gamma(y)\rangle_X = \langle \mathbf{A}f, v_\gamma(y)\rangle_Y\,.$$

Thus, we can calculate f_γ by simply evaluating inner products of the measurement data $\mathbf{A}f$ with the *reconstruction kernels* $v_\gamma(y)$.

The first feature of the method can be seen from (21): The computation of the reconstruction kernels does not depend on the noise perturbed measurement data g. As a matter of fact in most cases, such as in computerized tomography and TCT (see section 5), we have an analytic expression for $v_\gamma(y)$ available. A further advantage of the procedure is the possibility to use invariance properties of the underlying operator $\mathbf{A}$ to enhance the effectivity considerably. In [21, 22] the authors developed a convergence and stability analysis for the method of approximate inverse in general Hilbert spaces which also applies to the inverse TCT problem.

5 Computation of reconstruction kernels

In this section we apply the method of generalized inverse to TCT in a spherical geometry.

Instead of trying to solve $\mathbf{P}f = p$ we search for smoothed approximations $(f_{\gamma,\nu})_{\gamma>0}$ of the form

$$f_{\gamma,\nu}(y) := \langle f, e_{\gamma,\nu}(\cdot,y)\rangle\,, \qquad y \in \mathbb{R}^3\,,$$

where we consider radially symmetric mollifiers $(e_{\gamma,\nu}(\cdot,y))_{\gamma>0}$ of the form

$$e_{\gamma,\nu}(x,y) = \frac{1}{I_\nu \gamma^3} R_\nu\left(\frac{\|y-x\|^2}{\gamma^2}\right)\,, \qquad x,y \in \mathbb{R}^3\,. \tag{22}$$

Here, $\nu > 0$ is a real number, $I_\nu := \pi^{3/2}\Gamma(\nu+1)/\Gamma(\nu+5/2)$ is a scaling factor and R_ν is a function on $[0,\infty)$ defined by

$$R_\nu(s) := \begin{cases} (1-s)^\nu\,, & \text{if } 0 \le s \le 1\ , \\ 0\,, & \text{if } s \ge 1\ . \end{cases} \tag{23}$$

Since $\operatorname{supp}(R_\nu) = [0,1]$ it follows that $e_{\gamma,\nu}(\cdot,y)$ has support $\overline{B_\gamma(y)}$ and by the chain rule we see that $e_{\gamma,\nu}(\cdot,y) \in C^k(\mathbb{R}^3)$ for all integer numbers $k < \nu$. Let us now show that

$$\int_{B_\gamma(y)} e_{\gamma,\nu}(x,y)\, dx = 1\,, \qquad y \in \mathbb{R}^3\,. \tag{24}$$

By using spherical coordinates $z = y + \eta\gamma\sigma$ with $\eta \in [0,1]$ and $\sigma \in S^2$ we can see that

$$\int_{B_\gamma(y)} e_{\gamma,\nu}(x,y)\, dx = \frac{1}{I_\nu}\int_0^1 \int_{S^2} R_\nu(\eta^2)\, d\Omega(\sigma)\, \eta^2\, d\eta = \frac{4\pi}{I_\nu}\int_0^1 (1-\eta^2)^\nu \eta^2 d\eta$$

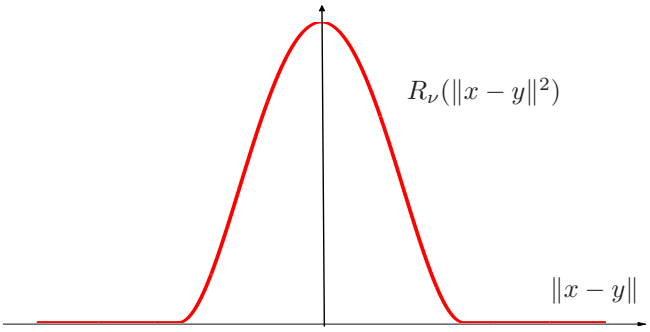

Figure 4: The mollifier $e_{\gamma,\nu}(\cdot, y)$ for $\gamma = 1$ and $\nu = 2$.

Substituting $\eta = \cos\alpha$ yields

$$\int_{B_\gamma(y)} e_{\gamma,\nu}(x,y)\,dz = \frac{4\pi}{I_\nu}\int_0^{\pi/2} \sin^{2\nu+1}(\alpha)\cos(\alpha)\,d\alpha = \frac{4\pi}{I_\nu}\frac{\Gamma(\nu+1)\Gamma(3/2)}{2\Gamma(\nu+5/2)}\,.$$

For the last equality we have used [3, formula 16, p. 993]. Hence (24) follows from the definition of I_ν and the identity $\Gamma(3/2) = \sqrt{\pi}/2$. Thus, $e_{\gamma,\nu}$ is a mollifier, i.e., satisfying (17), (18), (19).

From corollary 3.5 we deduce that if $e_{\gamma,\nu}(\cdot, y)$ and $tD_t\mathbf{N}e_{\gamma,\nu}(\cdot, y)$ are C^1 functions then

$$v_{\gamma,\nu}(y) := \frac{2}{\rho}tD_t\mathbf{N}e_{\gamma,\nu}(\cdot, y) \tag{25}$$

is a solution of the equation $-\mathbf{N}^*D_tv_{\gamma,\nu}(y) = e_{\gamma,\nu}(\cdot, y)$. From Lemma 3.3 it follows that if $\tau \ll 1$ we can approximate $\mathbf{P}^*v_{\gamma,\nu}(y)$ by $-\mathbf{N}^*D_tv_{\gamma,\nu}(y)$ and therefore we can regard $v_{\gamma,\nu}(y)$ as a reconstruction kernel for the operator $\mathbf{P}$ associated to the mollifier $e_{\gamma,\nu}(\cdot, y)$.

In order to compute (25) we have to calculate $D_t\mathbf{N}f$ where f is a translation of a rotationally symmetric function. This is subject of lemma 5.1 and theorem 5.2.

Lemma 5.1. *Let $\varphi : [0,\infty) \to \mathbb{R}$ be continuous and Φ be a primitive of φ. Assume $y \in \mathbb{R}^3$ and define $f_\varphi \in C^0(\mathbb{R}^3)$ by $f_\varphi(x) := \varphi(\|x-y\|^2)$. Then*

$$(\mathbf{M}f_\varphi)(x,t) = \begin{cases} \frac{\Phi\left((\|x-y\|+t)^2\right)-\Phi\left((\|x-y\|-t)^2\right)}{4t\|x-y\|}\,, & \text{if } x \neq y\,, \\ \varphi(t^2)\,, & \text{if } x = y\,. \end{cases} \tag{26}$$

for positive t, $x \in \mathbb{R}^3$ and $\mathbf{M}f_\varphi(x,0) = \varphi(\|x-y\|^2) = f_\varphi(x)$.

Proof. The identity $\mathbf{M}f_\varphi(x,0) = \varphi(\|x-y\|^2)$ immediately follows from the definitions of f_φ and $\mathbf{M}$ (see (10)).

Now let $t > 0$ and $x \in \mathbb{R}^3$. If $x = y$ then $f_\varphi(x + t\omega)$ is constant on $\omega \in S^2$ and hence $\mathbf{M}f_\varphi(x,t) = \varphi(t^2)$. If $x \neq y$ then

$$\begin{aligned} \mathbf{M}f_\varphi(x,t) &= \frac{1}{4\pi}\int_{S^2} \varphi(\|x+t\omega-y\|^2)\,d\Omega(\omega) \\ &= \frac{1}{4\pi}\int_{S^2} \varphi\left(\|x-y\|^2 + t^2 + 2t\|x-y\|\left\langle\frac{x-y}{\|x-y\|},\omega\right\rangle\right)d\Omega(\omega)\,. \end{aligned}$$

To evaluate the last integral we can apply the *Funck-Hecke theorem* for $n = 3$, see e.g. [20, p. 20], and we obtain

$$\mathbf{M}f_\varphi(x,t) = \frac{1}{2}\int_{-1}^{1} \varphi(\|x-y\|^2 + t^2 + 2t\|x-y\|s)\,ds\,.$$

Since Φ is a primitive of φ we find by the substitution rule

$$\begin{aligned}\mathbf{M}f_\varphi(x,t) &= \frac{\Phi(\|x-y\|^2+t^2+2t\|x-y\|s)\big|_{-1}^{1}}{4t\|x-y\|} \\ &= \frac{\Phi\left((\|x-y\|+t)^2\right)-\Phi\left((\|x-y\|-t)^2\right)}{4t\|x-y\|}\,.\end{aligned}$$

Hence we have proved (26). □

Theorem 5.2. *Let φ, Φ, and f_φ be as in lemma 5.1 and assume that φ is a C^1 function such that there is some $0<\gamma<1$ with $\operatorname{supp}(\varphi)\subseteq[0,\gamma^2]$. Further assume that $y\in B_{\rho-\gamma}$. Then $f_\varphi\in C_c^1(B_\rho)$, $D_t\mathbf{N}f_\varphi\in C_c^1(S_\rho\times[0,2\rho])$ and*

$$(D_t\mathbf{N}f_\varphi)(\sigma,t)=p_\varphi(\|\sigma-y\|,t)\,,\qquad \sigma\in S_\rho\,,\quad t\in[0,2\rho]\,, \tag{27}$$

where

$$p_\varphi(s,t):=\frac{(s-t)\varphi\left((s-t)^2\right)}{2s}\,,\qquad s>0\,,\quad t\in[0,2\rho]\,. \tag{28}$$

Proof. Since $\|\cdot\|^2\in C^\infty(\mathbb{R}^n)$ it follows by the chain rule that $f_\varphi=\varphi\circ\|\cdot\|^2\in C^1(\mathbb{R}^3)$. To show that $\operatorname{supp}(f_\varphi)\subset\subset B_\rho$ let $\eta:=(\|y\|+\gamma+\rho)/2$ and $x\in\mathbb{R}^3\setminus B_\eta$. From $\|y\|<\rho-\gamma$ we see that $0<\eta<\rho$ and thus $B_\eta\subset\subset B_\rho$. From the triangle inequality it follows that $\|x-y\|\geq\|x\|-\|y\|\geq\eta-\|y\|=(\rho+\gamma-\|y\|)/2>0$ and hence $f_\varphi(x)=0$. This shows that $f_\varphi\in C_c^1(B_\rho)$.

Next we verify equation (27). Let $t>0$ and $\sigma\in S_\rho$. Since $(\mathbf{N}f_\varphi)(\sigma,t)=(t\mathbf{M}f_\varphi)(\sigma,t)$ and $\|\sigma-y\|>\gamma>0$ it follows from lemma 5.1 that

$$(D_t\mathbf{N}f_\varphi)(\sigma,t)=\frac{\partial}{\partial t}\left(\frac{\Phi\left((\|\sigma-y\|+t)^2\right)-\Phi\left((\|\sigma-y\|-t)^2\right)}{4\|\sigma-y\|}\right)\,. \tag{29}$$

Since $\|\sigma-y\|+t>\gamma$ the first term on the right hand side vanishes. Moreover, since φ is the derivative of Φ, equation (29) implies (27). For $t=0$ equation (27) holds true since both sides vanish.

Finally the assertion $D_t\mathbf{N}f_\varphi\in C_c^1(S_\rho\times[0,2\rho])$ is a direct consequence of equations (27), (28). □

We are now able to compute an explicit representation of $v_{\gamma,\nu}(y)$.

Corollary 5.3. *Let $v_{\gamma,\nu}(y)$ be defined by (25) with $e_{\gamma,\nu}(\cdot,y)$ as in (22), (23) and let $\nu>1$. Further assume $y\in B_{\rho-\gamma}$ and $0<\gamma<1$. Then we have the representation*

$$v_{\gamma,\nu}(y)(\sigma,t)=\frac{k_{\gamma,\nu}(\|\sigma-y\|,t)}{4\pi\|\sigma-y\|}\,,\qquad \sigma\in S_\rho\,,\quad t\in[0,2\rho]\,, \tag{30}$$

where

$$k_{\gamma,\nu}(s,t):=\frac{4\pi t(s-t)\rho}{\gamma^3 I_\nu}R_\nu\left((s-t)^2/\gamma^2\right)\,. \tag{31}$$

Particularily, if $\|\sigma-y\|\notin[t-\gamma,t+\gamma]$, then $v_{\gamma,\nu}(y)(\sigma,t)=0$.

Proof. The assumption $\nu>1$ guarantees that $\varphi(r^2)=R_\nu(r^2/\gamma^2)/(I_\nu\gamma^3)$ and hence $f_\varphi=e_{\gamma,\nu}(\cdot,y)$ satisfy the conditions claimed in theorem 5.2. Hence from equation (25) it follows that

$$\begin{aligned}v_{\gamma,\nu}(y)(\sigma,t) &= \frac{2}{\rho}\frac{t}{\gamma^3 I_\nu}\frac{(\|\sigma-y\|-t)R_\nu\left((\|\sigma-y\|-t)^2/\gamma^2\right)}{2\|\sigma-y\|} \\ &= \frac{1}{4\pi\|\sigma-y\|}\frac{4\pi t(\|\sigma-y\|-t)}{\rho\gamma^3 I_\nu}R_\nu\left((\|\sigma-y\|-t)^2/\gamma^2\right)\,.\end{aligned}$$

Hence we have proven (30), (31). From the fact that $\mathrm{supp}(R_\nu) = [0,1]$ it follows that $v_{\gamma,\nu}(y)(\sigma,t) = 0$ for $\|\sigma - y\| \notin [t-\gamma, t+\gamma]$. □

Now let $\gamma > 0$, $\nu > 1$, assume $y \in B_{\rho-\gamma}$ and define $p := \mathbf{P}f$. Taking into account that $\mathbf{P}^* v_\gamma(y) = -\mathbf{N} D_t v_\gamma(y)$ if j is replaced by the delta distribution we may consider (30) as an appropriate choice for the reconstruction kernel associated to the mollifier $e_{\gamma,\nu}$. Note that in this case we set $\tau = 0$. The method of approximate inverse applied to $\mathbf{P}f = p$ then reads as

$$\begin{aligned} f_{\gamma,\nu}(y) &= \langle \mathbf{P}f, v_{\gamma,\nu}(y)\rangle_{2\rho} = \int_{S_\rho} \int_0^{2\rho} p(\sigma,t) \frac{k_{\gamma,\nu}(\|\sigma - y\|, t)}{4\pi\|\sigma - y\|}\, dt\, d\Omega_\rho(\sigma) \\ &= \int_{S_\rho} \frac{1}{4\pi\|\sigma - y\|} \left(\int_0^{2\rho} p(\sigma,t) k_{\gamma,\nu}(\|\sigma - y\|, t)\, dt \right) d\Omega_\rho(\sigma) = (\mathbf{N}^* q_{\gamma,\nu})(y)\,, \end{aligned}$$

with

$$q_{\gamma,\nu}(\sigma, s) := \int_{s-\gamma}^{s+\gamma} p(\sigma,t) k_{\gamma,\nu}(s,t)\, dt \tag{32}$$

which represents an inversion scheme of *filtered backprojection type*.

Remark 5.4. *The assumption $y \in B_{\rho-\gamma}$ is not a significant restrict with respect to applications, since $0 < \gamma \ll 1$ and the support of f has in fact a positive distance from $\partial B_\rho = S_\rho$ in practical experiments.*

6 Numerical Experiments

In this section we show numerical experiments of recovering a function f from measurement data $p = \mathbf{P}f$. Let $\nu > 0$ be a fixed positive number.

In section 5 we have outlined that we can find approximations $f_{\gamma,\nu}(y) := \langle p, v_{\gamma,\nu}(y)\rangle_{2\rho}$ by firstly evaluating the *filtered signal* $q_{\gamma,\nu}$ defined by (32) and then evaluating the backprojection

$$f_{\gamma,\nu}(y) = (\mathbf{N}^* q_{\gamma,\nu})(y) = \frac{1}{4\pi} \int_{S_\rho} \frac{q_{\gamma,\nu}(\sigma, \|y - \sigma\|)}{\|y - \sigma\|}\, d\Omega_\rho(\sigma)$$

in every reconstruction point $y \in B_\rho$. Hence the algorithm consists of two steps: First we perform a filtering step and then we integrate over all spheres with center on S_ρ intersecting y. This last step is also called backprojection. This procedure is analogous to the *filtered backprojection algorithm* in classical x-ray CT.

For our numerical tests we assume $\rho = 1$, that is $S_\rho = S^2$. We further assume that the data are merely known for a finite number of $N_\theta N_\varphi$ detector points

$$\sigma_{k,l} = \begin{pmatrix} \cos(\theta_k)\cos(\phi_l) \\ \cos(\theta_k)\sin(\phi_l) \\ \sin(\theta_k) \end{pmatrix} \in S^2 = S_\rho\,, \quad k = 1, \ldots, N_\theta\,, \quad l = 1, \ldots, N_\phi\,,$$

with $\theta_k := -\pi/2 + \pi(k-1)/(N_\theta - 1)$ and $\phi_l := 2\pi(l-1)/N_\phi$, and the pressure signals at each detector point is sampled at N_t time steps

$$t_m = 2(m-1)/N_t\,, \quad m = 1, \ldots, N_t\,.$$

The aim is to evaluate $f_{\gamma,\nu}$ at $N := N_y^3$ points y_i, $i = 1, \ldots, N$, lying on an equidistant grid. This requires the computation of $q_{\gamma,\nu}(\sigma_{k,l}, \|\sigma_{k,l} - y_i\|)$ in every reconstruction point y_i. To reduce the computational effort we evaluate $q_{\gamma,\nu}(\sigma_{k,l}, \cdot)$ for t_m with $m = 1, \ldots, N_t$ only and use linear interpolation to approximately find the value at $\|\sigma_{k,l} - y_i\|$. As quadrature rule on S^2 for a function F on the sphere we use the trapezoidal rule in θ and ϕ direction applied

to the coordinate representation $\cos(\theta)F(\theta,\phi)$. Hence our algorithm for the determination of $\mathtt{f}[i] := f_{\gamma,\nu}(y_i)$ out of the discrete data $\mathtt{p}[k,l,m] := p(\sigma_{k,l}, t_m)$ reads as follows:

Algorithm 1 Reconstruction of $\mathtt{f}[i]$ from measuring data $\mathtt{p}[k,l,m]$.

$\mathtt{const} \leftarrow 4\pi/(\gamma^3 I_\nu)$
$\mathtt{f}[1,...,N] \leftarrow 0$ ▷ initialization

for $m, m' = 1, \ldots, N_t$ **do** ▷ calculating kernel
  $\mathtt{k}[m,m'] \leftarrow \mathtt{const} \cdot t_m(t_{m'} - t_m) R_\nu\left((t_m - t_{m'})^2/\gamma^2\right)$
end for

for $k = 1, \ldots, N_\theta$, $l = 1, \ldots, N_\phi$ **do**
  $\mathtt{d\Omega} \leftarrow \cos(\theta_k) 2\pi^2/(N_\phi N_\theta)$

  for $m = 1, \ldots, N_t$ **do** ▷ filtering step
    $\mathtt{q}[m] \leftarrow 2/N_t \cdot \sum_{m'} \mathtt{k}[m,m']\mathtt{p}[k,l,m']$
  end for

  for $i = 1, \ldots, N$ **do**
    `Find` $m \in \{1, \ldots, N_t - 1\}$ `with` $t_m \le \|\sigma_{k,l} - x_i\| < t_{m+1}$
    $\mathtt{u} \leftarrow N_t(\|\sigma_{k,l} - x_i\| - t_m)/2$
    $\mathtt{Q} \leftarrow (1 - \mathtt{u}) \cdot \mathtt{q}[m] + \mathtt{u} \cdot \mathtt{q}[m+1]$ ▷ interpolation
    $\mathtt{f}[i] \leftarrow \mathtt{f}[i] + \mathtt{Q}/(4\pi\|x_i - \sigma_{k,l}\|) \cdot \mathtt{d\Omega}$ ▷ discrete backprojection
  end for

end for

The total number N_{op} of operations needed to perform this algorithm can easily be estimated. Let us assume that $O(N_\theta) = O(N_\phi) = O(N_t) = O(N_y)$. Then

$$N_{\mathrm{op}} = O(N_t^2) + O(N_\theta N_\phi)\Big(O(N_t^2) + O(N_y^3)\Big) = O(N^{5/3})\,.$$

We demonstrate the performance and stability of our algorithm by means of the following two examples:

1. Let us consider an energy deposition function $f \in C_c^1(B_\rho)$ of the form

$$f(y) = \sum_{\alpha=1}^{M} F_\alpha(\|y - y_\alpha\|)$$

consisting of M radially symmetric absorbers $f_\alpha(y) := F_\alpha(\|y - y_\alpha\|)$ with center y_α and radial profile F_α. From theorem 5.2 it follows that $p = \sum_\alpha p_\alpha$ is given by

$$p_\alpha(\sigma, t) = \frac{\|\sigma - y_\alpha\| - t}{2\|\sigma - y_\alpha\|} F_\alpha\left(|\|\sigma - y_\alpha\| - t|\right)$$

for $\sigma \in S^2$ and $t \ge 0$.

To produce the results of Figure 5 we have used an object consisting of 5 radially symmetric objects of different sizes. The algorithm was performed with $N_y = N_t = N_\phi = 120$ and $N_\theta = 60$. Figure 5 shows both the reconstruction out of the exact data and out of the data with a random perturbation of 20% additive Gaussian noise. The regularization parameter γ was chosen to be 0.05 and the exponent in the mollifier $\nu = 2$.

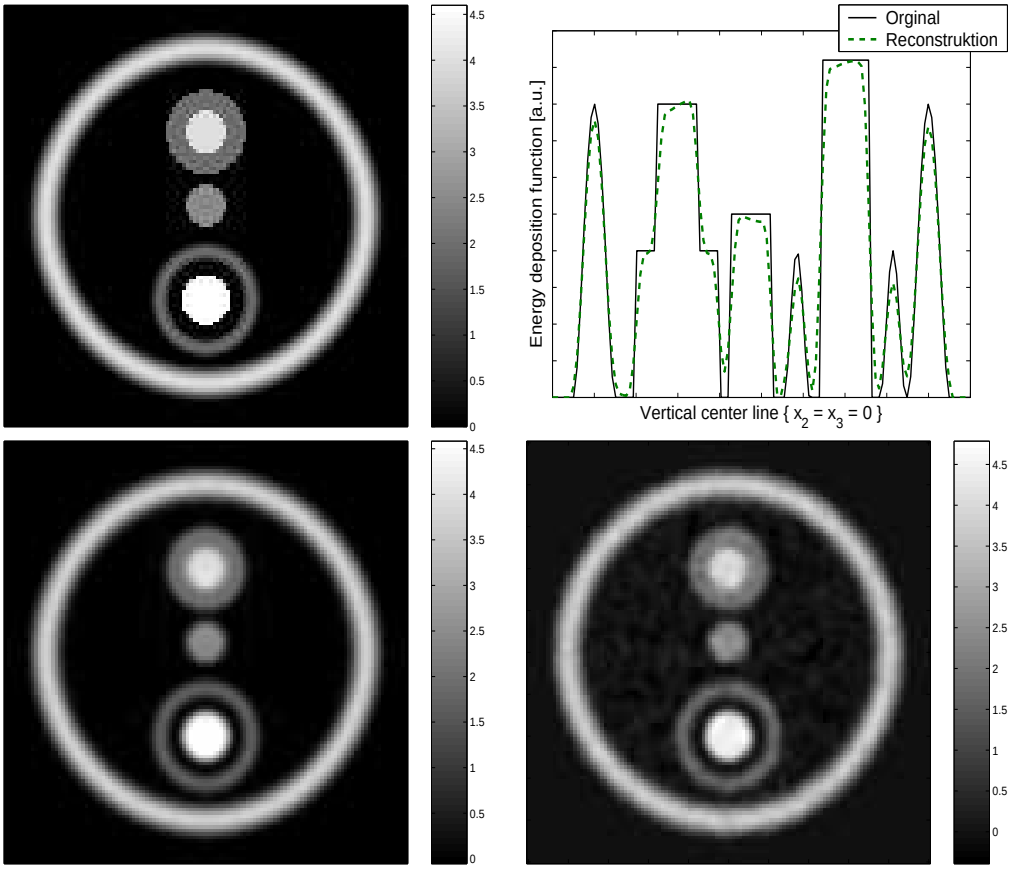

Figure 5: Top Left: Cross section of the synthetic data from which the thermoacoustic pressure is calculated analytically. Top right: Vertical centerline of the original and the reconstruction from exact data. Bottom Left: Reconstruction from exact data. Bottom Right: Reconstruction from noisy data perturbed with 20% Gaussian white noise.

2. Consider an arbitrary energy deposition function $f \in C_c^1(B_\rho)$. To simulate the measurement data we have to find $p(\sigma, t)$ for $\sigma \in S^2$ and $t \in [0, 2]$ numerically. Therefore we use the Fourier series expansions

$$f(y) = \frac{1}{8} \sum_{k \in \mathbb{Z}^3} f_k e^{-i\pi\langle k,y\rangle/2}\,, \tag{33}$$

and

$$p(y,t) = \frac{1}{8} \sum_{k \in \mathbb{Z}^3} p_k(t) e^{-i\pi\langle k,y\rangle/2}\,, \tag{34}$$

for $y \in [-2, 2]^3$ and $t \geq 0$. It is easy to see, that if we define

$$p_k(t) = \cos(\pi\|k\|t/2) f_k\,, \tag{35}$$

then p agrees with the unique solution of (7), (8) on $S^2 \times [0, 2]$ (for $\tau \to 0$). On the basis of (33), (34), (35) we compute approximations to $p = D_t \mathbf{N} f$ with help of the `FFT`-Algorithm.

In that way we simulated the thermoacoustic measurement data for a three dimensional head phantom. Figure 6 shows the head phantom and its reconstruction using algorithm 1. It was performed with $N_y = N_t = N_\phi = 100$, $N_\theta = 80$, $\gamma = 0.05$ and $\nu = 2$.

7 Conclusion

In the paper we have applied the method of approximate inverse to thermoacoustic tomography in a spherical scanning geometry. We were able to find analytical expressions of the reconstruction kernels for the considered radially symmetric mollifiers. The complexity of the resulting reconstruction algorithm is the same as for the filtered backprojection algorithm used to invert the classical Radon transform. Reconstructions from simulated measurement data have been given and show its validity. Future work will contain an detailed error analysis of discretization and interpolation.

Acknowledgement

The work of M.H. and O.S. has been supported by Österreichischen Fonds zur Förderung der wissenschaftlichen Forschung, Project Y123-INF.

References

[1] H. Abdullah and A.K. Louis. The Approximate Inverse for Solving an Inverse Scattering Problem for Acoustic Waves in an Inhomogeneous Medium. *Inverse Problems*, 15:1213–1230, 1999.

[2] D. T. Blackstock. *Fundamentals of theoretical acoustics*. Wiley-Interscience, Toronto, 2000.

[3] I. N. Bronstein, K.A. Semendjajew, G. Musiol, and H. Mühlig. *Taschenbuch der Mathematik*. Harri Deutsch, Frankfurt am Main, 1997.

[4] A. J. Chorin and Y. E. Marsden. *A mathematical introduction to fluid mechanics*. Springer, New York, 3 edition, 1993.

[5] D. Finch, S. K. Patch, and Rakesh. Determining a function from its mean values over a family of spheres. *SIAM J. Math. Anal.*, 35:1213–1240, 2004.

[6] V. E. Gusev and A. A. Karabutov. *Laser Optoacoustics*. Institute of physics, New York, 1993.

[7] M. Haltmeier, O. Scherzer, P. Burgholzer, and G. Paltauf. Thermoacoustic computed tomography with large planar receivers. *Inverse Problems*, 20:1663–1673, 2004.

[8] F. John. *Partial Differential Equations*. Springer, Berlin-New York, 1982.

[9] W. Joines, Y. Zhang, C. Li, and R. Jirtle. The measured electrical properties of normal and malignant human tissues from 50 to 900 mhz. *Med. Phys.*, 21:547–550, 1994.

[10] K. P. Köstli, D. Frauchinger, J. J. Niederhauser, G. Paltauf, H. W. Weber, and M. Frenz. Optoacoustic imaging using a three-dimensional reconstruction algorithm. *IEEE Journal in Quantum electronics*, 7(6), 2001.

[11] R.A. Kruger, W.L. Kiser, K.D. Miller, and H.E. Reynolds. Thermoacoustic ct: Imaging principles. *Proc SPIE*, 3916:150–159, 2000.

[12] R.A. Kruger, K.M. Stantz, and W.L. Kiser. Thermoacoustic ct of the breast. *Proc. SPIE*, pages 521–525, 4682.

[13] L. D. Landau and E. M. Lifschitz. *Lehrbuch der theoretischen Physik, Band VI: Hydrodynamik*. Akademie Verlag, Berlin, 1991.

[14] P. Liu. Image reconstruction from photoacoustic pressure signals. *Proc. SPIE*, 2681:285–296, 1996.

[15] A.K. Louis. Approximate inverse for linear and some nonlinear problems. *Inverse Problems*, 12:175–190, 1996.

[16] A.K. Louis. A unified approach to regularization methods for linear ill-posed problems. *Inverse Problems*, 15:489–498, 1999.

[17] A.K. Louis. Filter design in three-dimensional cone beam tomography: circular scanning geometry. *Inverse Problems*, 19:S31–S40, 2003.

[18] A.K. Louis and P. Maass. A mollifier method for linear operator equations of the first kind. *Inverse Problems*, 6:427–440, 1990.

[19] A.K. Louis and T. Schuster. A novel filter design technique in 2D computerized tomography. *Inverse Problems*, 12:685–696, 1996.

[20] Claus Müller. *Spherical harmonics*. Lecture Notes in Mathematics. Springer, Berlin-New York, 1966.

[21] A. Rieder and T. Schuster. The approximate inverse in action II. *Math. Comp.*, 72:1399–1415, 2003.

[22] A. Rieder and T. Schuster. The approximate inverse in action III: 3D-Doppler tomography. *Numerische Mathematik*, 97:353–378, 2004.

[23] T. Schuster. The 3D Doppler transform: elementary properties and computation of reconstruction kernels. *Inverse Problems*, 16(3):701–723, 2000.

[24] T. Schuster. An efficient mollifier method for three-dimensional vector tomography: convergence analysis and implementation. *Inverse Problems*, 17:739–766, 2001.

[25] T. Schuster, J. Plöger, and A.K. Louis. Depth-resolved residual stress evaluation from X-ray diffraction measurement data using the approximate inverse method. *Zeitschrift für Metallkunde*, 94(8):934–937, 2003.

[26] T. Schuster and E.T. Quinto. On a regularization scheme for linear operators in distribution spaces with an application to the spherical Radon transform. to appear in SIAM J. Appl. Math., URL: `http://www.num.uni-sb.de/iam/schusterP.php`, 2004.

[27] M. Xu, D. Feng, and L.-H. Wang. Exact frequency-domain reconstruction for thermoacoustic tomography-I: Planar geometry. *IEEE Trans. Med. Imag.*, 21(7):823–828, 2002.

[28] M. Xu and L.-H. Wang. Time-domain reconstruction for thermoacoustic tomography in a spherical geometry. *IEEE Trans. Med. Imag.*, 21(7):814–822, 2002.

[29] Y. Xu, M. Xu, and L.-H. Wang. Exact frequency-domain reconstruction for thermoacoustic tomography-II: Cylindrical geometry. *IEEE Trans. Med. Imag.*, 21(7):829–833, 2002.

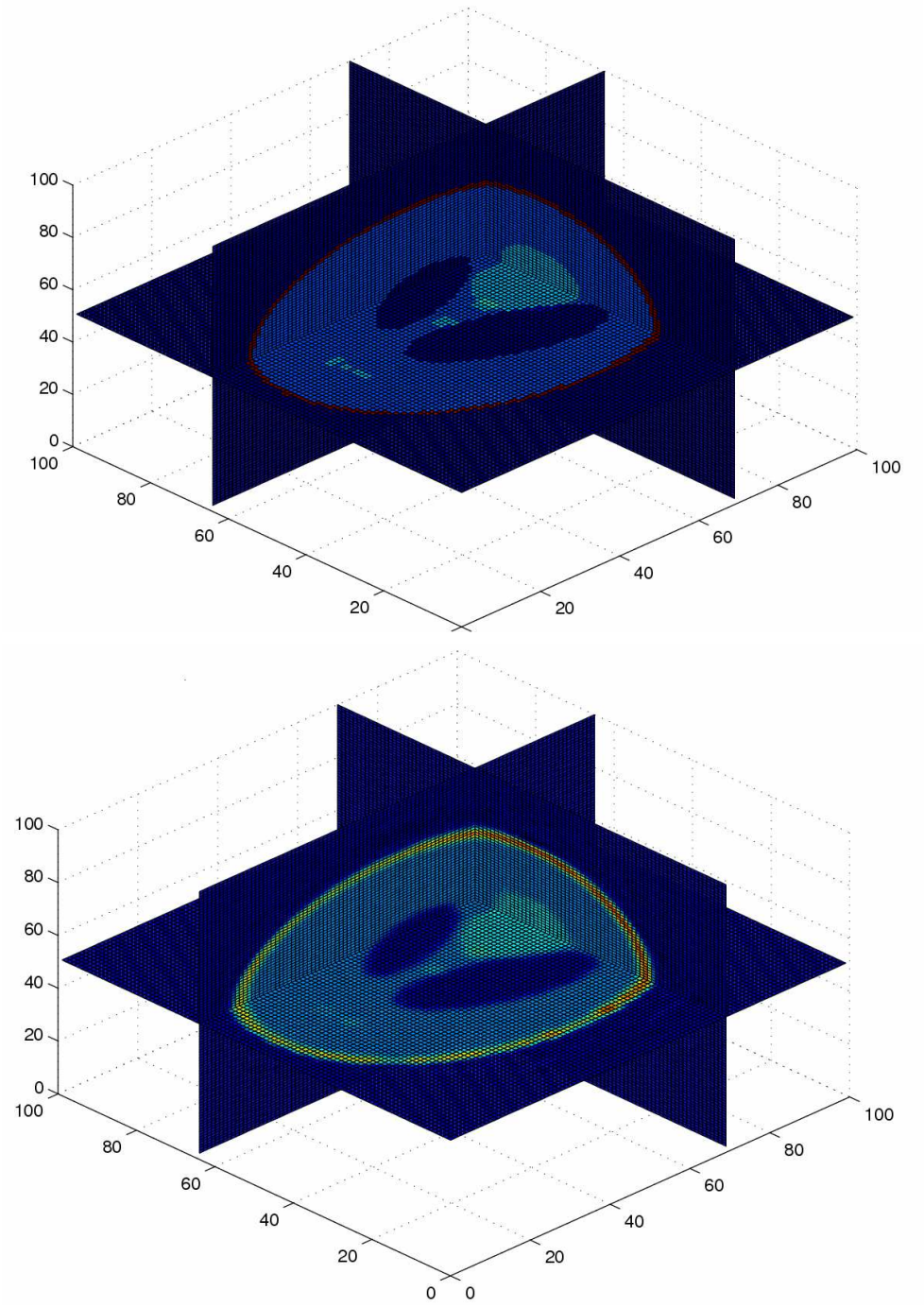

Figure 6: TOP: Synthetic data from which the thermoacoustic pressure is calculated numerically. BOTTOM: Reconstruction from simulated data with $\gamma = 0.05$ and $\nu = 2$.